J Adv Ceram

Research Article

Realizing intense deep-far-red broadband emission derived from mica ceramics through isomorphic cation substitution/doping for plant cultivation lighting and latent fingerprint identification

Mengrou Jiang[1,†], Na Qi[1,†], Yufeng Mao[1], Ji Zhou[2,✉], Lianshe Fu[3], Shikao Shi[1,✉]

Cite this article: Jiang M, Qi N, Mao Y, et al. *J Adv Ceram* 2026, **15**(3): 9221254. https://doi.org/10.26599/JAC.2026.9221254

ABSTRACT: The exploration of transition metal Mn^{2+}-activated luminescent materials is gaining increasing interests due to their diverse uses. Herein, Mn^{2+}-incorporated fluorphlogopite (FP; $KMg_3AlSi_3O_{10}F_2$) mica ceramics were successfully prepared by a high-temperature solid-state reaction process, in which Mn^{2+} occupied the Mg^{2+} site through isomorphic substitution. The FP itself and derived Mn-mica ($KMg_{2.5}Mn_{0.5}AlSi_3O_{10}F_2$) possess negligible luminescence under ultraviolet (UV) excitation. However, the doping of rare earth Eu^{2+} into Mn-mica generates an evident deep-far-red broadband emission at approximately 620–860 nm, peaking at 720 nm when excited with 240–360 nm, which is ascribed to the intrinsic $^4T_1 \rightarrow {}^6A_1$ transition of Mn^{2+}, and the maximum spectral enhancement reaches approximately 22-fold when excited with 320 nm. The more dramatic result is that the complete substitution of Na^+ for K^+ in Mn-mica ($NaMg_{2.5}Mn_{0.5}AlSi_3O_{10}F_2$) not only results in an enlarged excitation range toward the near-UV region but also greatly enhances the deep-far-red emission (more than 12-fold) under 365 nm excitation. After optimization, the luminescence internal quantum yield (QY) is 87.4%, and the emission intensity at 423 K retains 78% of that at ambient temperature, indicating that the modified mica ceramics have superior luminescence and thermal stability through the cooperative effects of isomorphic cation substitution and doping, which is applicable for plant cultivation lighting and latent fingerprint identification.

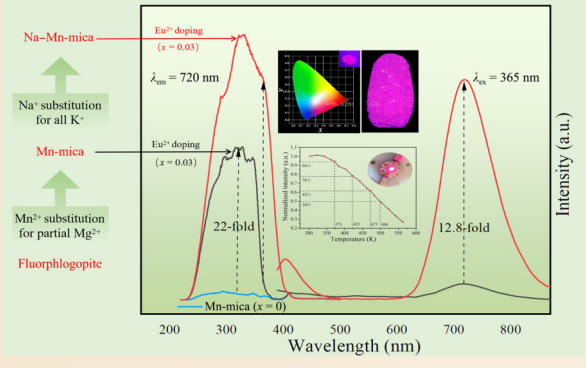

KEYWORDS: mica ceramics; luminescence; transition metal Mn^{2+}; rare earth Eu^{2+}; isomorphic cation substitution/doping

1 Introduction

During the last few decades, spectral conversion materials in the deep-red (620–700 nm), far-red (700–760 nm) and near-infrared (760–1000 nm) regions have shown attractive prospects in phosphor-converted light-emitting diodes (pc-LEDs), bioimaging and diagnostics, food quality monitoring, and other photofunctional fields [1–6]. Notably, advancements in environmental agriculture have promoted the adoption of pc-LEDs as light sources for plant growth in popular greenhouse facilities [7,8]. In comparison with traditional lighting sources, pc-LEDs exhibit prominent merits of long work duration, effective energy savings and customized spectral range [9,10]. At present, there is increased interest in the design, fabrication and improvement of near-ultraviolet (UV) excited deep-far-red phosphors [11,12]. However, the available red phosphors, such as $CaAlSiN_3$:Eu^{2+} nitride, K_2SiF_6:Mn^{4+} fluoride, and Y_2O_2S:Eu^{3+} oxysulfide, suffer from shortcomings, such as severe preparation conditions, low chemical stability, weak luminescence or an unmatched emission range [13–15], which limit their practical use in plant cultivation lighting. It is crucial to develop novel deep-red and far-red phosphors with a suitable emission wavelength range, high quantum efficiency, superior chemical and heat stability, and environmental friendliness.

The transition metal Mn^{2+} ion, as a promising emission center, has been extensively incorporated into inorganic compounds for the use of lighting and diverse fields. Since Mn^{2+} has a $3d^5$ electronic configuration in which 3d electrons are located in the

† Mengrou Jiang and Na Qi contributed equally to this work.

[1] College of Chemistry and Materials Science, Hebei Key Laboratory of Inorganic Nanomaterials, Hebei Normal University, Shijiazhuang 050024, China. [2] School of Materials Science and Engineering, State Key Lab of New Ceramics and Fine Processing, Tsinghua University, Beijing 100084, China. [3] Department of Physics, CICECO–Aveiro Institute of Materials, University of Aveiro, Aveiro 3810-193, Portugal.

✉ Corresponding authors. E-mail: J. Zhou, zhouji@tsinghua.edu.cn; S. Shi, shishikao@hebtu.edu.cn

Received: December 2, 2025; Revised: January 5, 2026; Accepted: January 19, 2026

outermost layer of the atomic orbital, the resulting d–d transitions are quite sensitive to the host surroundings, and the emission wavelength depends closely on the magnitude of the crystal field. Mn^{2+} typically shows green luminescence in a weak crystal field (tetrahedral coordination site) and red light emission in a strong crystal field (octahedral coordination site) [16–19]. At present, Mn^{2+}-activated ceramic phosphors can be categorized into a few systems, such as oxides (including phosphate, borate, silicate, and perovskite oxides) [20–22], nitrides [23], oxynitrides [24], and halides (including fluorides and chlorides) [25–27]. To the best of our knowledge, Mn^{2+}-activated oxyfluoride phosphors, particularly those with layered structures, are still seldom explored.

Mica ceramics, as a representative clay mineral with strong insulation strength and high heat and corrosion resistance, have been widely applied in electronic communication and industry fields. However, naturally occurring mica ceramics have difficulty meeting practical demands in luminescence owing to their nonuniform purity and quality [28]. With a unique layered structure and isomorphic substitution features, synthetic-mica ceramics can be fabricated through high-temperature solid-state reactions and exhibit considerable variation in physical and chemical properties. For example, the OH^- anion in natural mica ceramics (phlogopite, $KMg_3AlSi_3O_{10}(OH)_2$) can be readily replaced with F^- due to their close ionic radius and the same valence state and can form synthetic-mica ceramics with higher heat resistance [29]. At present, the most popular synthetic-mica in industry is $KMg_3AlSi_3O_{10}F_2$ oxyfluoride, which is generally called fluorphlogopite (FP) [30]. In the layered structure of FP (Fig. 1(e)), each sheet is composed of two SiO_4 tetrahedra and one MgO_6 octahedron (tetrahedron–octahedron–tetrahedron (T–O–T)) unit, and the adjacent T–O–T units are connected with the interlayer K^+ cation, in which K^+ can be exchanged with similar cations such as Na^+ or Ba^{2+}. Recently, our group successfully prepared rare earth Sm^{3+}-doped $NaMg_{2.5}Si_4O_{10}F_2$ (sodium tetrasilicate FP) and Eu^{3+}-doped $BaMg_2Si_4O_{10}F_2$ (barium tetrasilicate FP) ceramic powders, and their luminescence properties were investigated [31,32]. After structural modification, the characteristic red sharp-line emissions of Sm^{3+} ($^4G_{5/2} \rightarrow {}^6H_{7/2}$) and Eu^{3+} ($^5D_0 \rightarrow {}^7F_2$) were greatly enhanced in comparison with that in the original FP, and their potential applications in latent fingerprint identification were explored because mica ceramics have superb adhesion and desirable photothermal stability.

In this work, the transition metal Mn^{2+} was used as an emission center to partially substitute for Mg^{2+} in mica ceramics. Owing to the close ion radii and same valence states of Mn^{2+} and Mg^{2+} cations, Mn^{2+} ions would easily occupy the MgO_6 octahedral site in mica ceramics and perhaps emit the typical red light according to the crystal field theory. The crystal structure and luminescence properties of the mica ceramic powders were analyzed with X-ray diffraction (XRD), scanning electron microscopy (SEM), X-ray photoelectron spectroscopy (XPS), and photoluminescence (PL) characterization. The FP itself and derived Mn-mica (in which Mn^{2+} substitutes for partial Mg^{2+}) possess negligible luminescence when excited with UV light. However, the doping of tiny Eu^{2+} into Mn-mica results in an evident deep-far-red broadband emission, which originates from the intrinsic $^4T_1 \rightarrow {}^6A_1$ transition of Mn^{2+}. To our much surprise, the deep-far-red broadband emission is extremely enhanced under near-UV 365 nm excitation by using Na^+ cation complete substitution for K^+. The modified mica ceramics integrate superior luminescence, wide UV-near-UV excitation range, strong adhesion, and desirable thermal stability. The related mechanism is discussed in detail, and the application prospects of mica ceramics are explored in the fields of plant cultivation lighting and latent fingerprint identification.

2 Experimental

2.1 Materials and fabrication

Mn^{2+}- and Eu^{2+}-incorporated mica ceramic powders were fabricated by a conventional high-temperature solid-state reaction, in which K_2SiF_6 (A.R.), Na_2SiF_6 (A.R.), MgO (A.R.), Al_2O_3 (A.R.), SiO_2 (A.R.), $MnCO_3$ (A.R.), and Eu_2O_3 (99.99%, Beijing Institute of Nonferrous Metals, China) were used as raw materials. Owing to the close ionic radius, the Mn^{2+} and Eu^{2+} cations should occupy Mg^{2+} and K^+/Na^+ sites in the host lattice, respectively. In accordance with the following chemical equations: $K_{1-x}Eu_xMg_{3-y}Mn_yAlSi_3O_{10}F_{2+x}$ (x = 0–0.05, y = 0–0.75, Mn-mica series), $Na_{1-x}Eu_xMg_{3-y}Mn_yAlSi_3O_{10}F_{2+x}$ (x = 0–0.05, y = 0–0.75, Na–Mn-mica series), and $(Na_zK_{1-z})_{1-x}Eu_xMg_{2.5}Mn_{0.5}AlSi_3O_{10}F_{2+x}$ (x = 0.03, z = 0–1.0, Na–K–Mn-mica series), the raw materials were weighed in the stoichiometric ratio and ground thoroughly in an agate mortar. Then, the mixtures were heated at 1150 °C for 5 h in a tube furnace with a reducing atmosphere (N_2 + C powder (A.R.)). Finally, the furnace was cooled to room temperature, and the samples were reground into ceramic powders for collection.

Additionally, the FP and Na-FP ($NaMg_3AlSi_3O_{10}F_2$) host as well as Eu^{2+}-doped (x = 0.03) FP and Na-FP were also prepared in a similar way for the convenience of comparison.

The optimal Eu^{2+}-doped Mn-mica ceramic phosphor and epoxy resin were mixed according to a volume ratio of 1 : 1 and then coated on a 365 nm light emitting diode (LED) chip. For gelation, the LED device was kept in an oven at 60 °C for 2 h.

2.2 Measurements and characterization

XRD of the synthetic-mica ceramic powders was carried out with an X-ray powder diffractometer (Smart Lab, Rigaku, Japan) with Cu Kα radiation (λ =1.5406 Å) operating at 40 kV and 40 mA, employing a step size of 0.02° over a 2θ scan range of 5°–50°. The morphology images and elemental maps were obtained using a SEM (S-4800, Hitachi, Japan) field emission. XPS measurements were performed on a spectrometer (Kalpha XPS, Thermo, USA) to determine the chemical composition and valence state of Mn. The PL excitation/emission spectra of the mica ceramics were measured with a fluorescence spectrometer (FS5-TCSPC, Edinburgh Instruments, UK) equipped with a xenon lamp as an excitation source. The luminescence decay curves, internal quantum yield (QY), and temperature-dependent PL emission spectra were recorded using fluorescence spectrometer (FLS-980, Edinburgh, UK). Moreover, inductively coupled plasma-optical emission spectrometry (ICP-OES) was performed on an ICP-OES (iCAP 7400, Thermo, USA) to confirm the complete substitution of Na^+ for K^+ in Mn-mica.

3 Results and discussion

3.1 Structure, composition, and morphology

To clarify the isomorphic cation substitution of the activator Mn^{2+} for the Mg^{2+} site and Na^+/Eu^{2+} into the interlayer alkali metal K^+ site in the FP host, the ionic radius percentage difference (D_r) is calculated with Eq. (1):

$$D_r = \frac{R_m(CN) - R_d(CN)}{R_m(CN)} \times 100\% \quad (1)$$

where CN is the coordination number, and R_m(CN) and R_d(CN) represent the ionic radii of the host and the incorporated/doped ions, respectively [33]. In general, the incorporated ion can substitute for the host ion only when the D_r value is less than or

equal to 30% ($D_r \leq 30\%$) [34]. For Mn^{2+} (ionic radius (r) = 0.81 Å, CN = 6) and Mg^{2+} (r = 0.86 Å, CN = 6), the D_r value (Mn–Mg) is calculated to be only 5.81%, implying that Mn^{2+} substitutes for partial Mg^{2+} in the host with little distortion. For Na^+ (r = 1.53 Å, CN =12), Eu^{2+} (r = 1.49 Å, CN =12) and K^+ (r = 1.78 Å, CN =12), the D_r values for (Eu–Na), (Na–K), and (Eu–K) are 2.61%, 14.04%, and 16.29%, respectively. The results show that isomorphic substitution between Na^+ and K^+ readily occurs, and the tiny doped Eu^{2+} would occupy the interlayer Na^+ or K^+ sites without difficulty.

The crystal structure and phase purity of mica ceramic powders were identified by XRD patterns, and the typical XRD patterns relevant to FP, Mn-mica, Na-FP, Na–Mn-mica and Na–K–Mn-mica samples are given in Fig. 1. For the FP and Mn-mica series (Fig. 1(a)), the main peaks at approximately 8.9°, 19.3°, 26.8°, 34.1°, and 45.3° (2θ) are indexed to the (001), (100), (003), (112), and (005) planes, respectively, which match well with the standard card of FP (JCPDS#16-0352). For the Na-FP and Na–Mn–mica series (Fig. 1(b)), the main diffraction peaks at 9.2°, 19.4°, 27.7°, 34.2°, and 47.0° (2θ) also belong to the (001), (100), (003), (112), and (005) planes. However, the 2θ values corresponding to the (00l) (l = 1, 3, and 5) planes have all been enlarged compared to that of Fig. 1(a). This phenomenon can be more clearly observed in Fig. 1(c) for the XRD patterns of the Eu^{2+}-doped Na–K–Mn-mica series. With increasing Na^+ content (z value), the 2θ value corresponding to the (00l) (l = 1, 3, and 5) planes gradually shifts toward higher 2θ angles. As a result, the interlayer spacing for the layered mica (d value in Fig. 1) is accordingly decreased from 9.93 to 9.61 Å. The enlargement of diffraction peaks for the (l = 1, 3, and 5) planes and the decrease in interlayer spacing are all due to Na^+ with a smaller ionic radius substituting for K^+ sites in mica ceramic samples.

The diffraction peak positions and shapes for all the samples have similar features, in which the (001) and (003) crystal planes are dominant and the 2θ values corresponding to the (00l) (l = 1, 3, and 5) planes possess good multiple relationships, implying synthetic-mica ceramics with perfect layered structures. Moreover, the Rietveld refinement for the XRD pattern of Eu-doped Mn-

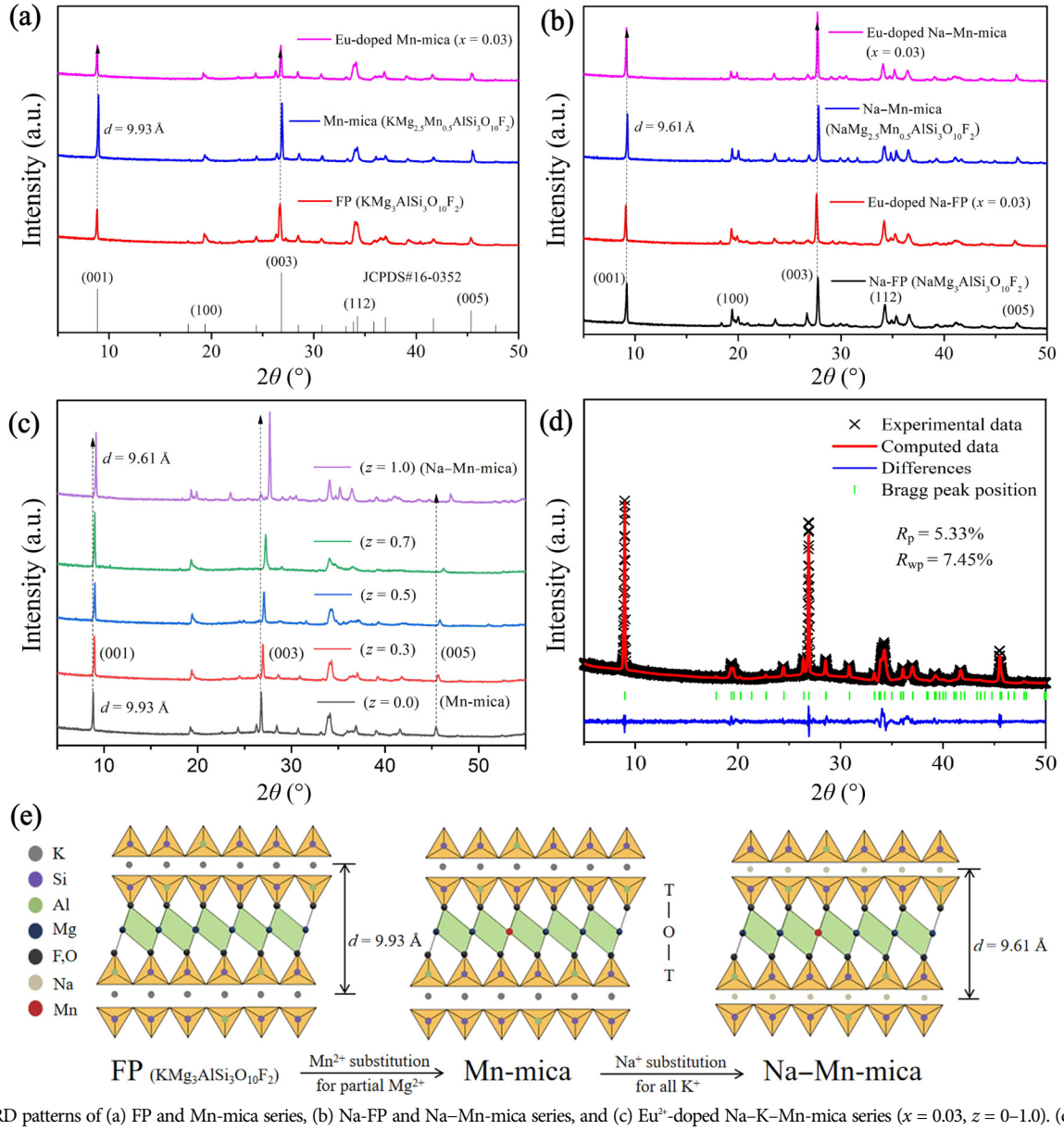

Fig. 1 XRD patterns of (a) FP and Mn-mica series, (b) Na-FP and Na–Mn-mica series, and (c) Eu^{2+}-doped Na–K–Mn-mica series (x = 0.03, z = 0–1.0). (d) Rietveld refinement of Eu-doped Mn-mica (x = 0.03, y = 0.50), and (e) schematic diagrams of lamellar structure for FP, Mn-mica, and Na–Mn-mica samples.

mica (x = 0.03, y = 0.50) is plotted in Fig. 1(d). The refinement result reveals that both R_p and R_{wp} factors (Two factors in Rietveld XRD refinement, which show the goodness of fit between the experimental and claculated data. The smaller the value, the better the fit) are quite small, which is in accordance with the FP monoclinic structure with the $C_{2/m}$ space group (Fig. S1 in the Electronic Supplementary Material (ESM)). The reason for this should be ascribed to the similar radius for Mn^{2+} with Mg^{2+} in six-coordinated MgO_6 surroundings and Eu^{2+} with K^+ ions in the interlayer. Calculated from Eq. (1), the D_r values 5.81% (Mn–Mg) and 16.29% (Eu–K) are much smaller than 30%. Therefore, Mn^{2+} and Eu^{2+} cations would substitute for Mg^{2+} in the T–O–T unit and alkali metal ions in the layer, respectively. After Mn^{2+} (y = 0.50) and tinny Eu^{2+} (x = 0.03) incorporation into the host, there is little shift in the main diffraction peaks, demonstrating the incorporation of Mn^{2+} and Eu^{2+} into the mica ceramic host through isomorphic cation substitution. Figure 1(e) plots schematic diagrams of the lamellar structure for the FP, Mn-mica, and Na–Mn-mica ceramic samples.

To analyze the morphology and composition of the as-prepared mica ceramic, SEM images of Eu^{2+}-doped Mn-mica and Na–Mn-mica are displayed in Figs. 2(a) and 2(b), respectively. The stacked sheet can be clearly observed, and the edge of the sheet presents obvious stratification, which is in agreement with the XRD results. The elemental mapping profiles in Figs. 2(c)–2(k) illustrate that Eu^{2+}-doped Na–Mn-mica contains Na, Mg, Mn, Al, Si, O, F, and Eu. Furthermore, the elemental mapping profiles of Eu^{2+}-doped Mn-mica are shown in supporting information Fig. S2 in the ESM, which are in line with the chemical composition of the compound.

To further determine the chemical composition and valence state of Mn in mica ceramics, the full XPS spectrum of Eu^{2+}-doped Na–Mn-mica is presented in Fig. 3(a). The elemental signals of the related chemical components Na, Mg, Mn, Al, Si, O, F, and Eu are all observed, which is in accordance with the elemental mapping profiles. The existence of carbon is mainly due to the adsorption of C from the reducing atmosphere (the introduction of C powder during the high-temperature solid-state reaction). Figure 3(b) shows the XPS high-resolution spectrum of the Mn 2p core level, in which two broad bands at 641 and 653 eV correspond to the Mn $2p_{3/2}$ and $2p_{1/2}$ orbitals, respectively. In particular, a satellite peak at 646 eV is observed, which originates from Mn^{2+} [35,36]. Therefore, the Mn in the mica ceramics should be present in the 2^+ state. The Eu^{2+}-doped Mn-mica ceramics have similar XPS results to those in Fig. 3, which is added to the supporting information in Fig. S3 in the ESM.

Moreover, the ICP-OES test on the Eu^{2+}-doped Na–Mn-mica was performed to further confirm the complete substitution of Na^+ for K^+ in Mn-mica, which is listed in the supporting information of Table S1 in the ESM.

3.2 Luminescence properties

The PL performances of Mn^{2+}- and Eu^{2+}-incorporated mica ceramic samples were investigated in detail. Figures 4(a)–4(d) plot the excitation and emission spectra of the Mn-mica ($K_{1-x}Eu_xMg_{2.5}Mn_{0.5}AlSi_3O_{10}F_{2+x}$, x = 0–0.05) and Na–Mn-mica ($Na_{1-x}Eu_xMg_{2.5}Mn_{0.5}AlSi_3O_{10}F_{2+x}$, x = 0–0.05) series. Without the introduction of Eu^{2+}, the deep-far-red emission band intensities of the samples are too weak (black lines in Figs. 4(a)–4(d)) to be hardly observed under the excitation of UV light. However, prominent excitation and emission bands appear after tiny Eu^{2+} doping. For the Eu^{2+}-doped Mn-mica ceramic samples, the excitation spectra (Fig. 4(a), emission wavelength in excitation spectrum (λ_{em}) = 720 nm) display similar wide bands from 240 to 360 nm with dominant excitation at approximately 290–350 nm, and the emission spectra (Fig. 4(b), excitation wavelength in

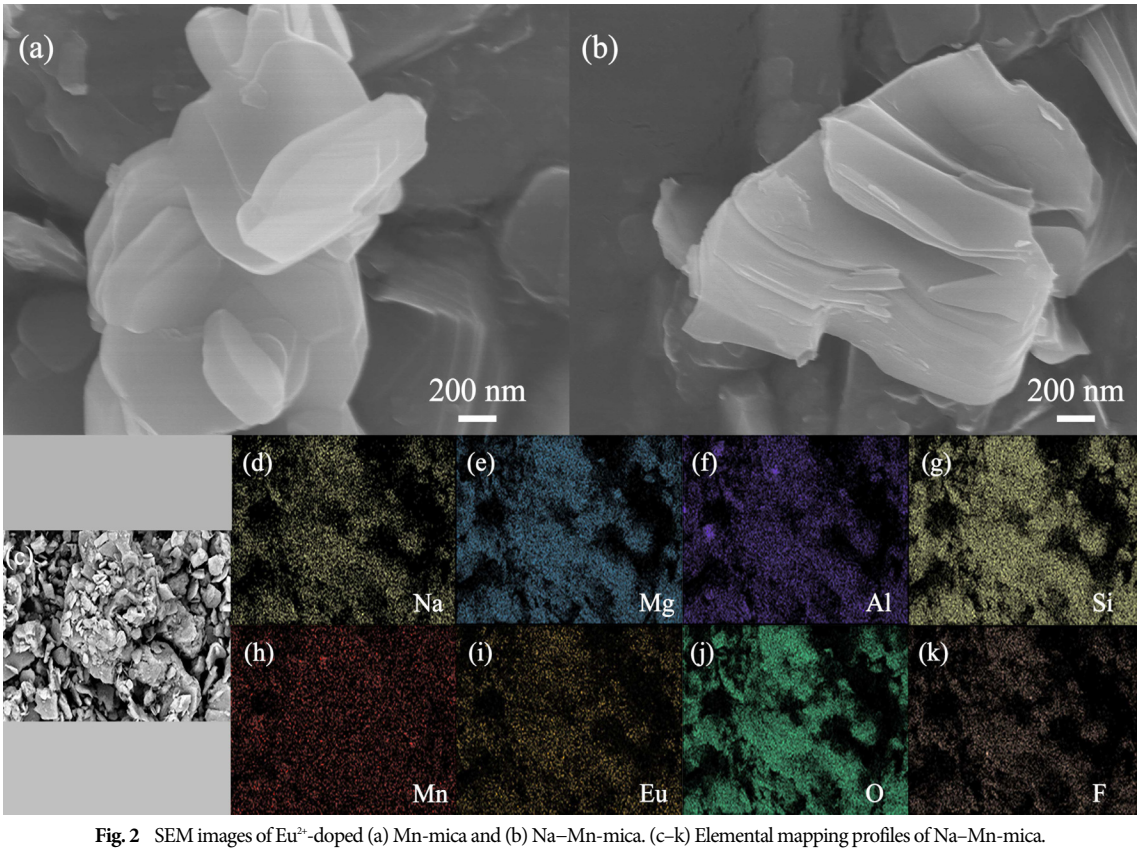

Fig. 2 SEM images of Eu^{2+}-doped (a) Mn-mica and (b) Na–Mn-mica. (c–k) Elemental mapping profiles of Na–Mn-mica.

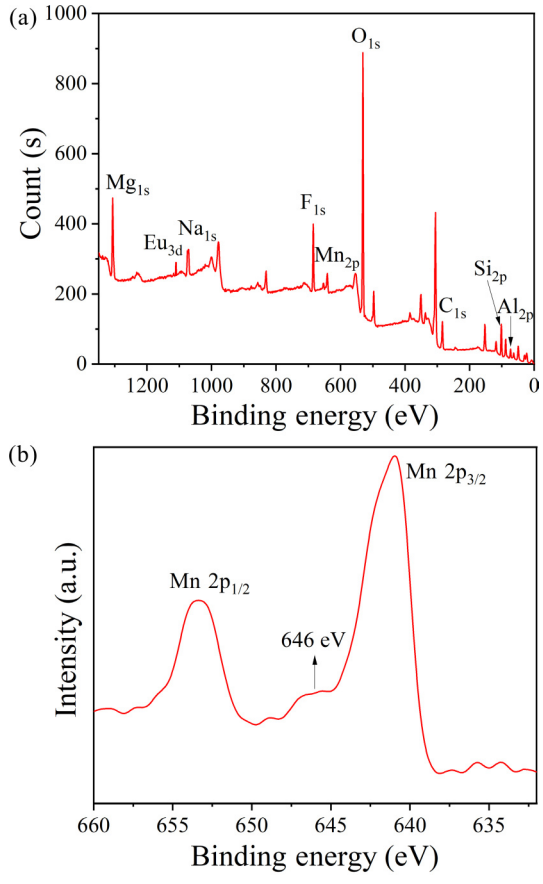

Fig. 3 (a) XPS full spectrum and (b) high-resolution spectrum of Mn 2p core level of Eu^{2+}-doped Na–Mn-mica.

emission spectrum (λ_{ex}) = 320 nm) possess two distinct broad bands at approximately 340–440 (violet-blue) and 620–860 nm (deep-far-red). The broad band at approximately 620–860 nm (deep-far-red) exhibits a peak at 720 nm with a full width at half maximum (FWHM) of 102 nm, which looks stronger than that in the violet-blue region (the peak is approximately 360–365 nm). For the Eu^{2+}-doped Na–Mn-mica ceramic samples, the excitation bands (Fig. 4(c), λ_{em} = 720 nm) are different from those in Fig. 4(a) because of a further shift toward near-UV to 400 nm. Excited with 320 nm, the emission spectra (Fig. 4(d)) also exhibit two separate broad bands, one at approximately 620–860 nm (deep-far-red), which is quite similar to that of Fig. 4(b), but the other in the violet-blue region, which is at approximately 370–480 nm with a peak at approximately 405 nm.

The deep-far-red emission bands at approximately 620–860 nm in Figs. 4(b) and 4(d) have almost the same FWHM and should be ascribed to the $^4T_1 \rightarrow {}^6A_1$ transition of Mn^{2+} because Mn^{2+} occupies six-coordinated surroundings through isomorphic substitution for Mg^{2+} [37]. It can be clearly observed that the excitation (λ_{em} = 720 nm) and deep-far-red emission band intensities all closely depend upon the Eu^{2+} doping concentration (x). As x = 0.01–0.03, the excitation and deep-far-red emission band intensities gradually increase with increasing x and reach the top at x = 0.03. Then, further increasing x to 0.04–0.05 results in a decrease in the emission band intensities. Therefore, the optimal Eu^{2+} doping concentration is concluded to be x = 0.03 for all mica ceramic samples. When excited with 320 nm and x = 0.03, the maximum emission intensities (approximately 720 nm) of Mn-mica and Na–Mn-mica are enhanced by approximately 22- and 210-fold, respectively, which means that doped Eu^{2+} plays a vital role in promoting Mn^{2+} red emission in mica ceramic samples.

The wide excitation bands of Figs. 4(a) and 4(c) as well as the emission bands in the violet-blue region of Figs. 4(b) and 4(d) are relevant to Eu^{2+} doping, which can be further confirmed through the PL results of Eu^{2+}-doped (x = 0.03) FP and Na-FP (Figs. 4(e) and 4(f)). Without the introduction of Mn^{2+}, the singly Eu^{2+}-doped FP and Na-FP exhibit quite similar excitation and violet-blue emission bands to those of the Mn-mica and Na–Mn-mica ceramic series. According to the crystal fields theory, the Eu^{2+} ion with the $4f^7$ configuration generally exhibits a broad absorption cross section in the excitation spectra owing to the parity-allowed nature of the $4f^7$–$4f^65d$ (4f–5d) transition and an electric-dipole allowed 5d–4f (d–f) transition band emission in inorganic materials [38,39]. The excitation bands (black lines in Figs. 4(e) and 4(f)) are ascribed to the 4f–5d absorption of Eu^{2+} [40], and the excitation band of Eu^{2+}-doped Na-FP is evidently shifted toward the near-UV region (~400 nm) compared to that of Eu^{2+}-doped FP (~360 nm). On the other hand, their emission spectra in the violet-blue region (blue line in Figs. 4(e) and 4(f)) also possess different features. The emission for Eu^{2+}-doped FP is practically composed of two interwoven narrow bands at approximately 340–440 nm, which originate from the 4f–4f (f–f) and 5d–4f (d–f) transitions of Eu^{2+}. In certain typical fluorides or oxide host surroundings, the lowest component of the $4f^65d$ configuration can shift to higher energy, so that the excited energy level ($^6P_{7/2}$) of the $4f^7$ configuration lies below it. As a result, the f–f narrow-band emission (approximately 360 nm) from the $^6P_{7/2} \rightarrow {}^8S_{7/2}$ (ground state) transition may occur and coexist with the d–f transition [41,42]. In this work, the mica ceramic host belongs to the oxyfluoride, and the f–f transition emission peak emerges as tiny Eu^{2+} is doped in the FP and Mn-mica series because the lowest excited position is at approximately 360 nm, which is quite close to the $^6P_{7/2}$ excited energy level of Eu^{2+}. However, as Eu^{2+} is doped in the Na-FP and Na–Mn-mica series, only the d–f transition emission band at approximately 360–480 nm with a peak at approximately 405 nm is observed. The reason for this is due to the lowest excited wavelength shifting to approximately 400 nm, which is much lower than that of the $^6P_{7/2}$ excited level of Eu^{2+}. In other words, Eu^{2+} doping in the Na-FP and Na–Mn-mica series results in a decrease in the lowest component of the $4f^65d$ configuration in comparison with that in the FP and Mn-mica series, and therefore, the excitation range is enlarged toward the near-UV region.

As shown in Fig. 4, the deep-far-red emission bands of Mn^{2+} in the Eu^{2+}-doped Mn-mica and Na–Mn-mica series samples are clearly observed under a large excitation range from the short-wavelength UV to near-UV region. In particular, the emission intensities for the Eu^{2+}-doped Na–Mn-mica series samples are dramatically enhanced when excited from 350 to 390 nm. Therefore, the selection of the excitation wavelength is a crucial factor in modulating the deep-far-red broadband emission intensities of mica ceramic samples.

Figures 5(a)–5(d) compare the excitation and emission intensities of the Eu^{2+}-doped (x = 0.03) Mn-mica and Na–Mn-mica samples. Despite the same Eu^{2+} doping concentration, the excitation band intensities for Na–Mn-mica are basically superior to those for Mn-mica (Fig. 5(a), λ_{em} = 720 nm). The enhanced extent depends closely upon the location of the excitation wavelength. When excited with a short wavelength of 254 nm, the deep-far-red emission is only somewhat enhanced (Fig. 5(b), λ_{ex} = 254 nm). Under medium-wavelength 320 nm excitation, the maximum emission enhancement is approximately 1.7-fold (Fig. 5(c), λ_{ex} = 320 nm). When excited with a long wavelength of 365 nm, the emission is extremely enhanced and reaches

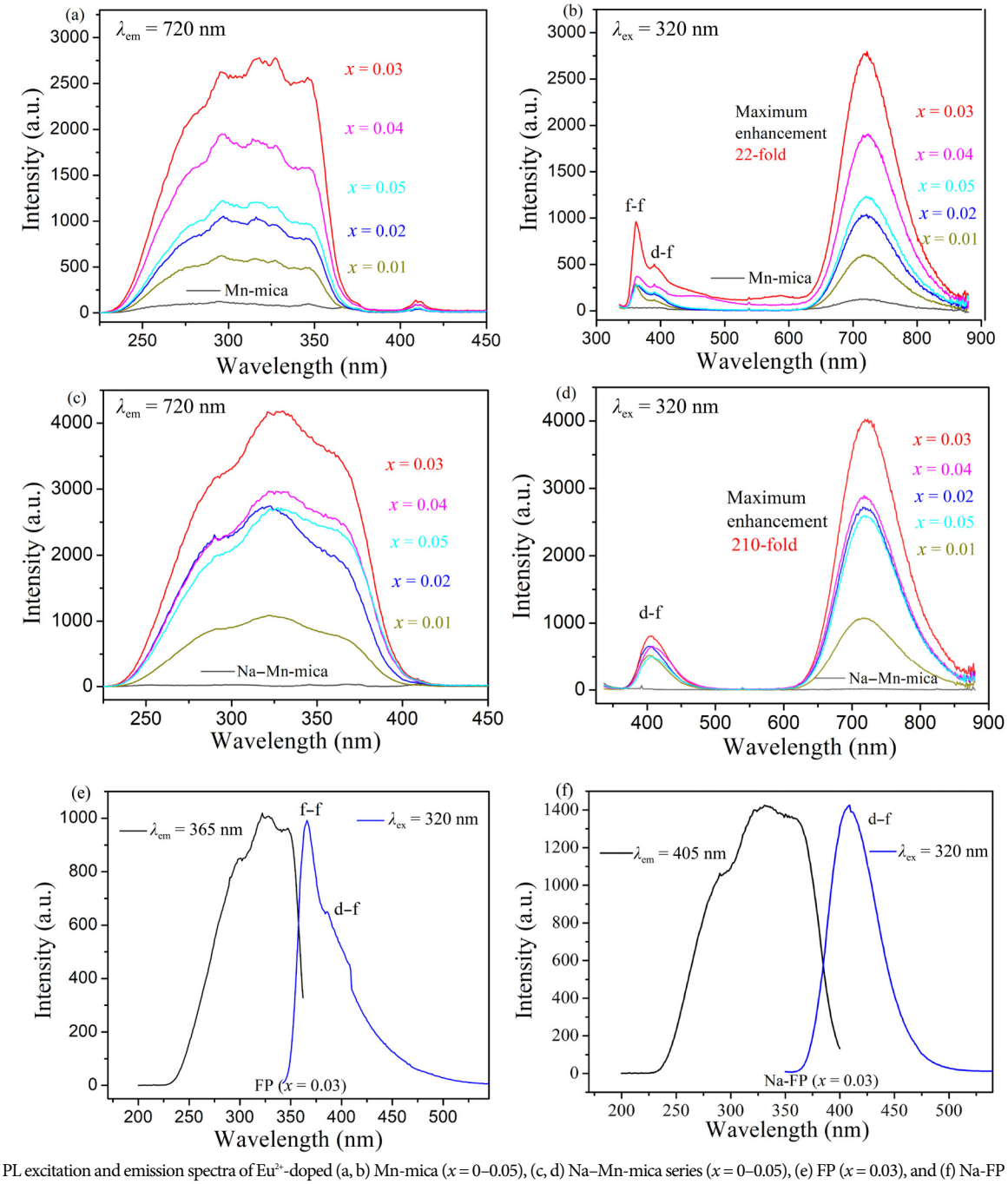

Fig. 4 PL excitation and emission spectra of Eu^{2+}-doped (a, b) Mn-mica (x = 0–0.05), (c, d) Na–Mn-mica series (x = 0–0.05), (e) FP (x = 0.03), and (f) Na-FP (x = 0.03).

approximately 12.8-fold (Fig. 5(d), λ_{ex} = 365 nm). Moreover, the dependence of the deep-far-red broadband emission intensity on the content of Na^+ substituting for K^+ (z = 0–1) in Mn-mica is also considered in Fig. 5(d). It can be clearly seen that the deep-far-red broadband emission intensity evidently increases with the increase in the z value and gets to the top as z = 1. This result firmly indicates that the complete substitution of Na^+ for K^+ in Mn-mica is beneficial for achieving the maximum enhanced luminescence of deep-far-red emission.

According to the PL data of Eu^{2+}-doped mica ceramics (Fig. 4), the tiny Eu^{2+} in the host first absorbs UV energy and then promotes the remarkable enhancement of the Mn^{2+} deep-far-red emission band. This implies that the effective energy transfer from Eu^{2+} (sensitizer) to Mn^{2+} (activator) should take place in the mica ceramic samples. To clarify the energy transfer phenomenon and optimize the Mn^{2+} content in synthetic-mica, the sensitizer Eu^{2+} doping concentration is kept stable (x = 0.03), the activator Mn^{2+} content (y) varies from 0.25 to 0.75 in the Mn-mica and Na–Mn-mica series, and their emission intensities are compared. In Fig. 6(a), the emission bands (λ_{ex} = 320 nm) of Eu^{2+}-doped Mn-mica are in agreement with Fig. 4(b), which contain the interwoven f–f and d–f transitions of Eu^{2+} at approximately 340–440 nm and the deep-far-red broadband of Mn^{2+} at approximately 620–860 nm. The increase in the activator Mn^{2+} content (y) leads to a monotonic reduction in Eu^{2+} emission intensities at approximately 340–440 nm and the subsequent enhancement of Mn^{2+} deep-far-red emission intensities at approximately 620–860 nm. The deep-far-red emission intensities reach a maximum at y = 0.50 and then obviously decrease with a further increase in y (y = 0.60, 0.75) due to concentration quenching. Similar phenomena also occur for the Eu^{2+}-doped Na–Mn-mica series, as shown in Fig. 6(b) (λ_{ex} = 365 nm). The

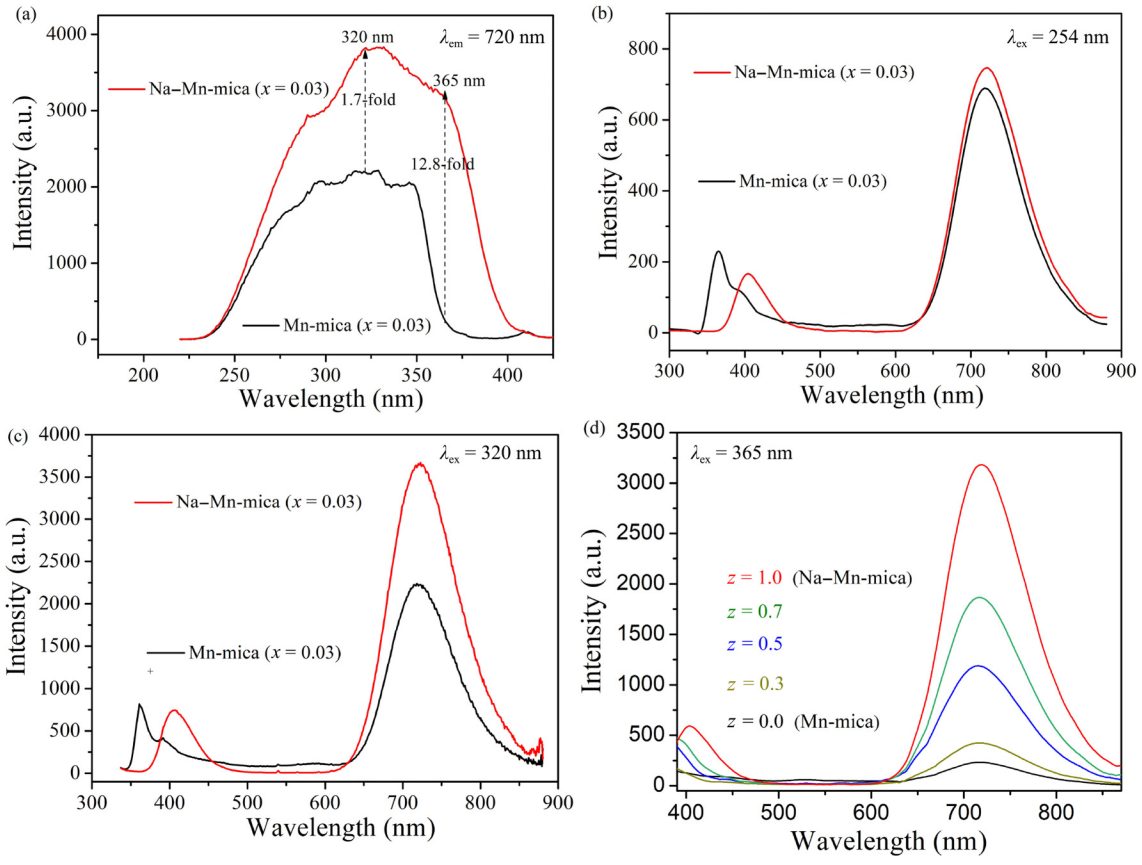

Fig. 5 Comparison of PL (a) excitation spectra (λ_{em} = 720 nm), (b) emission spectra (λ_{ex} = 254 nm), (c) emission spectra (λ_{ex} = 320 nm) of Eu^{2+}-doped Mn-mica and Na–Mn-mica (x = 0.03) samples, and (d) emission spectra (λ_{ex} = 365 nm) of Eu^{2+}-doped Na–K–Mn-mica series (x = 0.03, z = 0–1.0).

results demonstrate the successful transfer of Eu^{2+} excitation energy to Mn^{2+}, and the optimal Mn^{2+} content is y = 0.50.

It can be concluded from the above analysis that the optimal mica ceramic phosphor excited with near-UV 365 nm should be the Eu^{2+}-doped Na–Mn-mica sample, in which the Eu^{2+}-doping concentration x is 0.03 and the Mn^{2+} content y is 0.50. Therefore, the following discussion will mainly focus on the Eu^{2+}-doped Na–Mn-mica series.

The energy transfer mechanism involved in the sensitization process and the energy transfer efficiency between Eu^{2+} and Mn^{2+} in Eu^{2+}-doped Na–Mn-mica can be evaluated from the luminescence decay dynamics of Eu^{2+}. Figure 6(c) plots the luminescence decay curves (λ_{ex} = 358 nm, λ_{em} = 405 nm) of Eu^{2+} in the Na-FP (y = 0) and Na–Mn-mica (y = 0.25, 0.50, and 0.75) series ceramic samples. Without the incorporation of Mn^{2+}, the luminescence decay (black line) of Eu^{2+} exhibits a good linear relationship, indicating that Eu^{2+} mainly occupies a single lattice site when acting as the luminescent center in the crystal structure, and the decay is fitted with a typical single exponential function, whose fluorescence lifetime (τ_{s0}) can be simply calculated with Eq. (2):

$$I = A\exp\left(-\frac{t}{\tau_{s0}}\right) \quad (2)$$

where I represents the luminescent intensity at time (t), and A is a constant. Through Eq. (2), τ_{s0} is calculated to be 1.0 μs. With increasing Mn^{2+} content, the decay gradually becomes fast, and the decay curves deviate from the single exponential manner, which implies the activation of an additional de-excitation pathway for the Eu^{2+} 5d excited state through an energy transfer process [43]. The decay average lifetime (τ_s) follows the double exponential function [44] and can be calculated with Eqs. (3) and (4):

$$I(t) = A_1\exp\left(-\frac{t}{\tau_1}\right) + A_2\exp\left(-\frac{t}{\tau_2}\right) \quad (3)$$

$$\tau_s = \frac{A_1\tau_1^2 + A_2\tau_2^2}{A_1\tau_1 + A_2\tau_2} \quad (4)$$

where $I(t)$ is the PL emission intensity at time (t), A_1 and A_2 are constants, and τ_1 and τ_2 denote the fast and slow decay components of the fluorescent lifetime, respectively. The decay average lifetime (τ_s) of Eu^{2+}-doped Na–Mn-mica (y = 0.25, 0.50, and 0.75) decreases to 0.54, 0.39, and 0.30 μs with increasing Mn^{2+} content. The rapid decrease in the decay lifetime of Eu^{2+} in the Na–Mn-mica phosphors means that a nonradiative (NR) energy transfer process occurs from the sensitizer Eu^{2+} to the activator Mn^{2+}.

The energy transfer efficiency (η_{ET}) from the sensitizer Eu^{2+} to the activator Mn^{2+} can be calculated in accordance with Eq. (5) [45]:

$$\eta_{ET} = 1 - \frac{\tau_s}{\tau_{s0}} \quad (5)$$

where the η_{ET} values for the Eu^{2+}-doped Na–Mn-mica (y = 0.25, 0.50, and 0.75) are 46%, 61%, and 70%, respectively.

Figure 6(d) shows the energy level scheme of the energy transfer process from Eu^{2+} to Mn^{2+} in the Eu^{2+}-doped Na–Mn-mica samples. First, the electrons from the sensitizer Eu^{2+} were pumped to the $4f^65d$ excited state upon near-UV excitation. With some of the excited electrons returning to the $4f^7(^8S_{7/2})$ ground state, Na–Mn-mica emits violet-blue light. In the meantime, the electrons of the activator Mn^{2+} in the $^6A_1$ ground state were prompted to the $^4T_2$ excited state by a resonance energy transfer (RET) from the sensitizer Eu^{2+} owing to the similar energy gap between the $4f^65d$–$4f^7$ transition of Eu^{2+} and the $^4T_2 \rightarrow {}^6A_1$

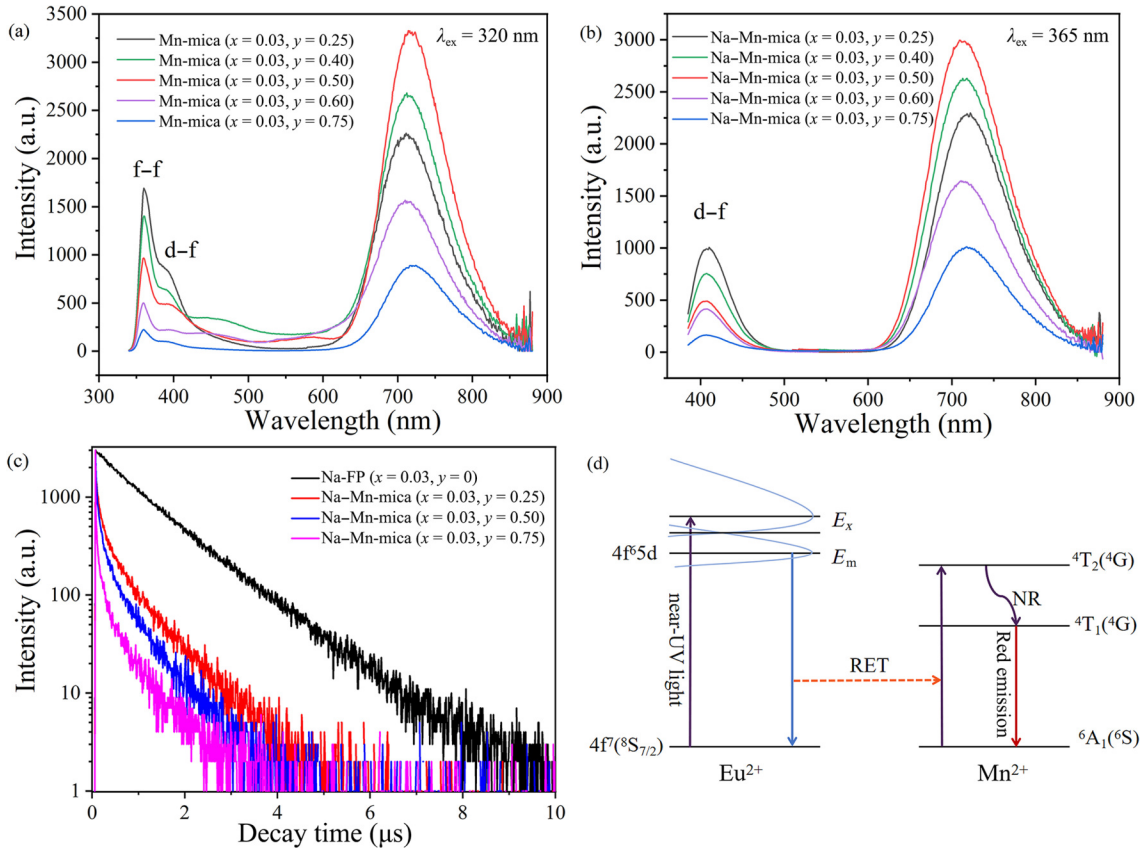

Fig. 6 (a) Emission spectra (λ_{ex} = 320 nm) of Eu^{2+}-doped Mn-mica (x = 0.03, y = 0.25–0.75), (b) emission spectra (λ_{ex} = 365 nm) of Eu^{2+}-doped Na–Mn-mica (x = 0.03, y = 0.25–0.75), (c) luminescence decay curves (λ_{em} = 405 nm) of Eu^{2+} in Na-FP (y = 0) and Na–Mn-mica (y = 0.25–0.75) series samples, and (d) schematic diagram of energy transfer process from Eu^{2+} to Mn^{2+} in Eu^{2+}-doped Na–Mn-mica samples.

transition of Mn^{2+} [46]. Then, the electrons from the $^4T_2$ state relax to the $^4T_1$ lower excited state of Mn^{2+} through a NR process and finally return to the $^6A_1$ ground state. Thus, the deep-far-red broadband emission from the $^4T_1 \rightarrow {}^6A_1$ transition of Mn^{2+} is greatly enhanced.

The luminescence QY, chromaticity coordinate and optical thermal stability are crucial factors to evaluate the applicability of phosphor materials in pc-LEDs. The internal QY of the optimal Eu^{2+}-doped Na–Mn-mica (x = 0.03, y = 0.50) was measured under 365 nm excitation (Fig. 7(a)) and is determined with Eq. (6):

$$QY = \frac{\int L_S}{\int E_R - \int E_S} \quad (6)$$

where L_S refers to the emission spectrum of the phosphor, and E_S and E_R denote the excitation spectra of the phosphor and $BaSO_4$ reference, respectively. The QY value is approximately 87.4%, which is much higher than those of recently reported Mn^{4+}-doped phosphors in double-perovskite structures (20%–40%) [47–49]. Figure 7(b) depicts the Commission International de L'Eclariage (CIE) chromaticity coordinate of the optimal Eu^{2+}-doped Na–Mn-mica ceramic phosphor. Under near-UV 365 nm excitation, the CIE chromaticity coordinate is (0.721, 0.279), which is located in the deep-far-red region. Moreover, the digital image of the Eu^{2+}-doped Na–Mn-mica ceramic phosphor is also given in the inset of Fig. 7(b) as irradiated with 365 nm light, indicating that the Eu^{2+}-doped Na–Mn-mica ceramic phosphor shows bright deep-far-red light when excited with near-UV 365 nm.

Figure 7(c) plots the temperature-dependent emission spectra (λ_{ex} = 365 nm) of the optimal Eu^{2+}-doped Na–Mn-mica ceramics from room temperature 303–563 K, in which the Mn^{2+} deep-far-red and Eu^{2+} violet-blue emission bands are quite similar to those in Fig. 4(d). With increasing testing temperature, all the deep-far-red and violet-blue emission band intensities are gradually reduced, exhibiting the typical high-temperature quenching effect due to the increase in the NR transition probability [50,51]. Furthermore, the deep-far-red emission peak blueshifts with increasing testing temperature, shifting from 720 to approximately 690 nm as the temperature is increased from room temperature 303 to 563 K. The temperature-induced emission peak blueshift may originate from the electron–phonon interaction between the ground state and excited state in the Mn^{2+} emission center, which needs to be further investigated. The dependence of the Mn^{2+} deep-far-red emission intensity on the testing temperature is displayed in Fig. 7(d). As the temperature increases to 373 K, the emission intensity remains at 94% of its initial value, indicating that the luminescence is quite stable from room temperature up to 373 K. After the testing temperature is raised to 423–473 K (the operation temperature of pc-LEDs), the relative emission intensity still retains 62%–78% of the initial value. Moreover, the quenching temperature ($T_{1/2}$), representing half of the initial intensity, reaches 500 K, which is much better than that of the Eu^{2+}-doped Mn-mica ceramic sample (Fig. S4 in the ESM) and recently reported Mn^{4+}-doped phosphors with a double-perovskite structure [9–11,46–48], confirming the optimal Eu^{2+}-doped Na–Mn-mica ceramic sample with excellent optical thermal stability.

Green plants perceive light through several organic pigments, which originate from photosynthetic prokaryotes. The deep-red (620–700 nm) and far-red light (700–760 nm) critically match the absorption zones of red phytochrome (Pr) and far-red phytochrome (Pfr), respectively [52]. To evaluate the performance

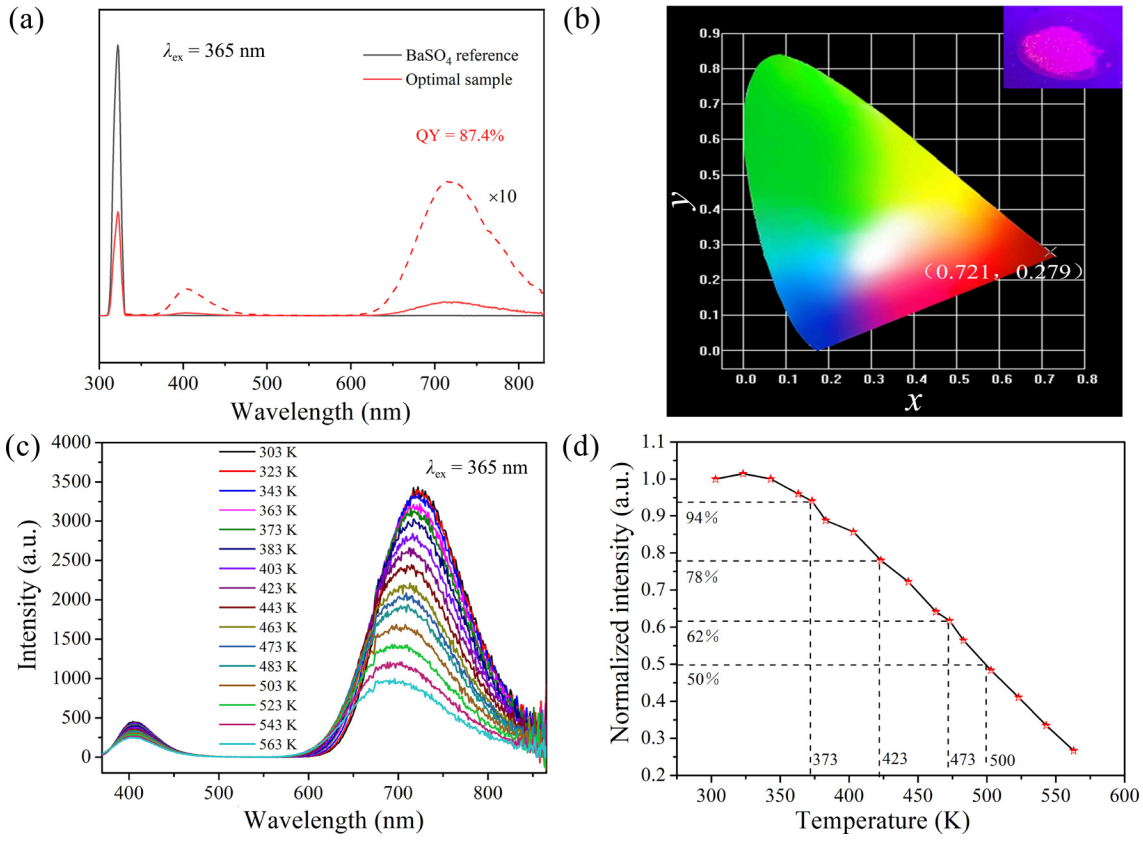

Fig. 7 (a) Internal QY, (b) CIE chromaticity coordinate, (c) temperature-dependent emission spectra (λ_{ex} = 365 nm), and (d) dependence of the Mn^{2+} deep-far-red emission intensity on the testing temperature of the optimal Eu^{2+}-doped Na–Mn-mica sample.

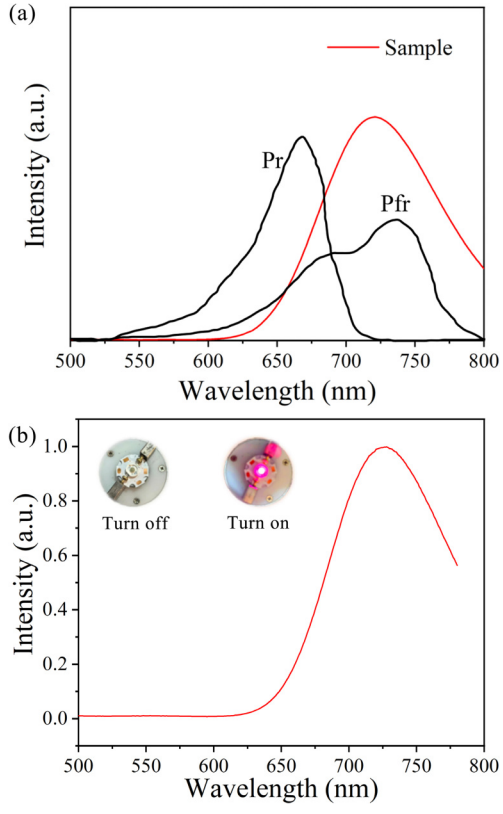

Fig. 8 (a) Comparison of emission spectrum of optimal Eu^{2+}-doped Na–Mn-mica sample with absorption curves of the plant pigments of Pr and Pfr and (b) emission spectrum of an LED device under a 60 mA driving current. Inset: digital photograph of the as-fabricated LED device.

of the synthetic-mica ceramic phosphor in practical uses, the emission spectrum of the optimal Eu^{2+}-doped Na–Mn-mica ceramic phosphor is compared with the absorption spectra of the plant Pr and Pfr (Fig. 8(a)). It can be seen that its emission range is highly matched with the absorption spectra of plant Pr and Pfr, which shows that the Eu^{2+}-doped Na–Mn-mica ceramic phosphor can be effectively used to prepare customized deep-far-red pc-LEDs for indoor plant cultivation.

The LED devices were successfully fabricated by coating the optimal Eu^{2+}-doped Na–Mn-mica ceramic phosphor on a 365 nm LED chip. Driven by a 60 mA current, the emission spectrum of the LED device is shown in Fig. 8(b). The electroluminescence emission spectrum clearly exhibits a deep-far-red emission band with a peak location at approximately 720 nm, which is almost the same as that of the PL result. Additionally, the inset of Fig. 8(b) also includes a digital photo of the LED, which emits bright red light at a 60 mA working current. By using pc-LEDs, near-UV light can be effectively converted into deep-far-red light, which endows the phosphor based on mica ceramics with great potential in the plant cultivation lighting field.

Moreover, latent fingerprint identification was also explored with Eu^{2+}-doped mica ceramic phosphors. Figures 9(a)–9(f) show the latent fingerprint images developed by Eu^{2+}-doped (x = 3 mol%) Mn-mica and Na–Mn-mica on tinfoil under irradiation with daylight, UV 254 nm, and near-UV 365 nm light, respectively. Owing to the mica with strong adhesive ability, the ceramic phosphors enable the observation of latent fingerprints under daylight (Figs. 9(a) and 9(d)), which is useful for rapid on-site investigation. Irradiated with 254 nm, the ceramic phosphor can emit the typical red light to highlight fingerprint contours, and the display effects are basically consistent (Figs. 9(b) and 9(e)), which is in accordance with the emission spectra of Fig. 5(b).

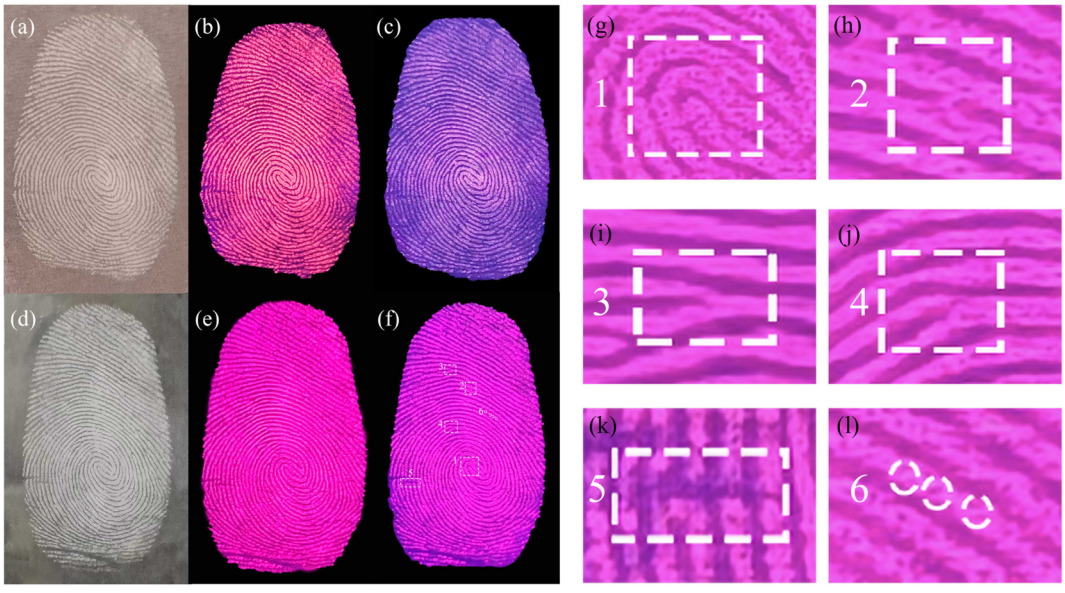

Fig. 9 Fluorescence images of latent fingerprints on tinfoil substrates under daylight, 254 and 365 nm light irradiation of Eu^{2+}-doped (a–c) Mn-mica and (d–f) Na–Mn-mica ($x = 0.03$, $y = 0.50$) and (g–l) magnified detailed images of latent fingerprint patterns on Na–Mn-mica under 365 nm near-UV light irradiation.

However, under near-UV 365 nm light irradiation, there is a marked difference in the luminescence performance of the ceramic phosphors (Figs. 9(c) and 9(f)). The Eu^{2+}-doped Mn-mica has relatively weak fluorescence signals, leading to the easy loss of key fingerprint information. In contrast, the Eu^{2+}-doped Na–Mn-mica displays extremely strong fluorescence brightness. Although the mica ceramic powders are uniformly distributed across the latent fingerprints, they are mainly attached to the ridges of the fingerprint rather than the furrows, resulting in fluorescence images with clearly distinguishable boundaries between ridges and furrows. On the other hand, the red fluorescence intensity is strong enough to resist background interference, including the light reflected from UV light into the substrates. Figures 9(g)–9(l) show magnified structural detail images (Fig. 9(f)) of the tinfoil substrate. In principle, the structural details of fingerprint ridges are classified into three levels, among which the level-2 and level-3 structural details are unique to individuals and possess individual identification. Not only are the level-1 details (whorl (Fig. 9(g)) clearly visible, but the level-2 (bridge (Fig. 9(h)), bifurcation (Fig. 9(i)) and ridge end (Fig. 9(j)) and level-3 details (scar (Fig. 9(k) and sweat pores (Fig. 9(l)) are also distinctly presented. It can be concluded that the Eu^{2+}-doped Na–Mn-mica ceramic phosphor exhibits high sensitivity in latent fingerprint development and holds potential application in this field.

4 Conclusions

In summary, a series of novel Eu^{2+}-doped Mn-mica and Na–Mn-mica ceramic phosphors derived from nonluminescent FP were successfully fabricated by a high-temperature solid-state reaction. All the synthetic-mica ceramic samples possess similar lamellar structures and morphologies. Owing to the close ionic radius and same valence state, Mn^{2+} and Na^+ would substitute for Mg^{2+} in six-coordinated MgO_6 lattice surroundings and K^+ sites sandwiched with T–O–T units through isomorphic cation substitution. The doped Eu^{2+} is liable to occupy the interlayer K^+ or Na^+ sites. Without the introduction of Eu^{2+}, both Mn-mica and Na–Mn-mica have almost negligible luminescence when excited with UV light. Nevertheless, the tiny Eu^{2+} doping results in a strong deep-far-red emission band at approximately 620–860 nm peaking at 720 nm with an FWHM of 102 nm when excited with UV light, which is ascribed to the intrinsic $^4T_1 \rightarrow {}^6A_1$ transition of Mn^{2+}. Under the optimal Eu^{2+} doping concentration (x = 0.03), the maximum emission intensity at approximately 720 nm (λ_{ex} = 320 nm) of Mn-mica and Na–Mn-mica is enhanced approximately 22- and 210-fold, respectively, which means that the doped Eu^{2+} plays a sensitizer role in promoting the activator Mn^{2+} red emission in mica ceramic samples. More interestingly, through the complete substitution of Na^+ for K^+, the Eu^{2+}-doped Na–Mn-mica ceramic phosphors exhibit an enlarged excitation range toward the near-UV region (to ~400 nm) and extremely enhanced deep-far-red broadband emission (more than 12-fold) under near-UV 365 nm excitation. The excited energy from the sensitizer Eu^{2+} to the activator Mn^{2+} involves a NR RET process due to the similar energy gap between the $4f^65d$–$4f^7$ transition of Eu^{2+} and the $^4T_2$–$^6A_1$ transition of Mn^{2+}. The optimal mica ceramic phosphor is Eu^{2+}-doped Na–Mn-mica, in which the Eu^{2+} doping concentration x is 0.03 and the Mn^{2+} content y is 0.50. The luminescence internal QY reaches 87.4%, and the emission intensity at 423 K (150 °C) retains 78% of that at ambient temperature, indicating that the modified synthetic-mica has superior luminescence and high optical thermal stability through the cooperative effects of isomorphic cation substitution and doping engineering. The intense deep-far-red broadband (620–860 nm) emission, wide UV excitation range (240–400 nm), desirable thermal stability and excellent adhesion endow the modified mica ceramic phosphor with tremendous potential for application in plant cultivation lighting and latent fingerprint identification.

Acknowledgements

This work was financially supported by the Southwest United Graduate School Research Program (No. 202302AO370008) and the Natural Science Foundation of China (No. 51972097). This work was also developed within the scope of the projects CICECO-Aveiro Institute of Materials (Nos. UIDB/50011/2020, UIDP/50011/2020, and LA/P/0006/2020), financed by national funds through the FCT/MCTES (PIDDAC). The authors would like to thank Prof. Xu Li from Hebei University for fabrication of pc-LED devices and electroluminescence measurements.

Availability of data and materials

The data that support the findings of this study are available from the corresponding author upon reasonable request.

Competing interests

The authors have no competing interests to declare that are relevant to the content of this article.

Electronic Supplementary Material

Supplementary material is available in the online version of this article at https://doi.org/10.26599/JAC.2026.9221254.

References

[1] Thejas KK, Abraham M, Kunti AK, *et al.* Review on deep red-emitting rare-earth free germanates and their efficiency as well as adaptability for various applications. *Appl Mater Today* 2021, **24**: 101094.

[2] Ma YL, Li XC, Wu L, *et al.* Preparation of $(Lu,Y)_3(Al,Sc,Cr)_2Al_3O_{12}$ phosphor ceramics with high thermal stability for near-infrared LED/LD. *J Adv Ceram* 2024, **13**: 354–363.

[3] Li CJ, Sójka M, Zhong JY, *et al.* Non-destructive food-quality analysis using near-infrared luminescence from $Mg_3Gd_2Ge_3O_{12}:Cr^{3+}$. *Dalton T* 2023, **52**: 12892–12898.

[4] Ge XF, Fu ZL. Multiwavelength responsive luminescence for temperature sensing and visualized information encoding/decoding based on Er^{3+}/Tb^{3+}-doped $Ba_2Ga_2GeO_7$ phosphors. *ACS Sustain Chem Eng* 2023, **11**: 6362–6372.

[5] Zhang SA, Long Y, Zhang PH, *et al.* Ultra-transparent β-$Ga_2O_3:Cr^{3+}$ glass-ceramics enabling high-efficiency true-transmission near-infrared light-emitting diodes. *J Adv Ceram* 2025, **14**: 9221075.

[6] Kamada Y, Hayasaka R, Uchida K, *et al.* Deep red photoluminescence from Cr^{3+} in fluorine-doped lithium aluminate host material. *Materials* 2024, **17**: 338.

[7] Yang J, Zha JH, Mao QN, *et al.* Achieving thermally stable $YAl_{3-x}Ga_x(BO_3)_4:Cr^{3+}$ near-infrared emitting phosphors via chemical substitution for plant growth LEDs. *Inorg Chem* 2024, **63**: 23999–24007.

[8] Chen ZL, Du SM, Zhu KM, *et al.* Mn^{4+}-activated double-perovskite-type Sr_2LuNbO_6 multifunctional phosphor for optical probing and lighting. *ACS Appl Mater Inter* 2023, **15**: 28193–28203.

[9] Sun ZG, Li JG, Qian HY, *et al.* Optical grade $(Gd_{0.95-x}Lu_xEu_{0.05})_3Al_5O_{12}$ ceramics with near-zero optical loss: Effects of Lu^{3+} doping on structural feature, microstructure evolution, and far-red luminescence. *J Adv Ceram* 2024, **13**: 113–123.

[10] Wang LL, Liu YG, Yu HJ, *et al.* Far-red-emitting Mn^{4+}-doped $Ca_2GdZr_2Al_3O_{12}$ phosphors for growing indoor plants. *J Lumin* 2022, **251**: 119132.

[11] Huang XY, Cen JL, Devakumar B, *et al.* High-brightness and high-color-purity red-emitting $Ca_8MEu(PO_4)_7$ (M = Mg and Zn) phosphate phosphors for near-UV-pumped pc-WLEDs. *Mater Today Chem* 2025, **43**: 102493.

[12] Chen SG, Du YF, Zhao HT, *et al.* Disorder–order transition and metal-to-metal charge transfer induced rare orangish-red emission in Bi^{3+}-activated double perovskite phosphors. *Chem Eng J* 2024, **502**: 157928.

[13] Uheda K, Hirosaki N, Yamamoto Y, *et al.* Luminescence properties of a red phosphor, $CaAlSiN_3:Eu^{2+}$, for white light-emitting diodes. *Electrochem Solid St* 2006, **9**: H22.

[14] Moon JW, Min BG, Kim JS, *et al.* Optical characteristics and longevity of the line-emitting $K_2SiF_6:Mn^{4+}$ phosphor for LED application. *Opt Mater Express* 2016, **6**: 782.

[15] Chou TW, Mylswamy S, Liu RS, *et al.* Eu substitution and particle size control of Y_2O_2S for the excitation by UV light emitting diodes. *Solid State Commun* 2005, **136**: 205–209.

[16] Su BB, Zhou GJ, Huang JL, *et al.* Mn^{2+}-doped metal halide perovskites: Structure, photoluminescence, and application. *Laser Photonics Rev* 2021, **15**: 2000334.

[17] Katayama Y, Kayumi T, Ueda J, *et al.* The role of Ln^{3+} (Ln = Eu, Yb) in persistent red luminescence in $MgGeO_3:Mn^{2+}$. *J Mater Chem C* 2017, **5**: 8893–8900.

[18] Adachi S. Review—Photoluminescence spectroscopy of Mn^{2+}-activated phosphors: Part I. Fundamentals. *ECS J Solid State Sc* 2023, **12**: 126003.

[19] Cornu L, Duttine M, Gaudon M, *et al.* Luminescence switch of Mn-doped $ZnAl_2O_4$ powder with temperature. *J Mater Chem C* 2014, **2**: 9512–9522.

[20] Dong LP, Zhang L, Xu YH, *et al.* Efficient red and broadband near-infrared luminescence in Mn^{2+}/Yb^{3+}-doped phosphate phosphor. *J Am Ceram Soc* 2021, **104**: 4109–4118.

[21] Song JZ, Zhao WR, Zhang HS, *et al.* Energy transfer and ratiometric Temperature sensing based on the dual-emitting $NaMgBO_3:Ce^{3+}$, Mn^{2+} phosphor. *J Lumin* 2021, **232**: 117858.

[22] Yu SM, Gong YJ, He GL, *et al.* Multimodal luminescence of $CaZnGe_2O_6:Mn^{2+},Yb^{3+}$ phosphors for anti-counterfeiting: Dynamic photoluminescence, afterglow, photostimulated luminescence, thermostimulated luminescence and mechanoluminescence. *Chem Eng J* 2025, **524**: 169152.

[23] Zhu KM, Chen ZL, Liu H, *et al.* Color-adjustable fluorescence and red persistent luminescence of rare earth-free $CaAlSiN_3$: Mn^{2+} phosphors prepared by combustion synthesis. *Opt Mater* 2023, **139**: 113765.

[24] Huo JS, Zhu QJ, Li SZ, *et al.* Effective assembly of a novel aluminum-oxynitride $BaAl_{11}O_{16}N$ activated by Eu^{2+} and Mn^{2+} via salt-flux assistance and its photophysical investigation. *J Alloys Compd* 2019, **787**: 96–103.

[25] Xu WX, Wang YB, Deng DG, *et al.* Improved X-ray excited optical luminescence of divalent manganese ion in $LiLuF_4$ nanoparticles via introducing energy transfer pathways. *J Lumin* 2022, **251**: 119197.

[26] Liu YF, Zhao J, Zhang Y, *et al.* Enhanced single-band red upconversion luminescence of α-$NaErF_4$: Mn nanoparticles by a novel hollow–shell structure under multiple wavelength excitation. *J Alloys Compd* 2019, **810**: 151761.

[27] Yan YH, Dai H, Li JK, *et al.* Narrow-band green-emitting Cs_3ZnCl_5: Mn^{2+} phosphors with abnormal thermal quenching. *J Lumin* 2023, **258**: 119821.

[28] Liu LD, Luo YY, Zhang Q, *et al.* Effect of MnO content on the crystallization, physicochemical and dielectric properties of mica glass-ceramics. *Ceram Int* 2022, **48**: 26732–26741.

[29] Chen AQ, Tan W, He HP, *et al.* Chemical and structural studies of coexisting 1M- and 2M1-polytypes in synthetic fluorophlogopites and influence of Al on the polytype formation. *Phys Chem Miner* 2019, **46**: 259–270.

[30] Wang YL, Lai XJ, Li HQ, *et al.* Significantly improve fire safety of silicone rubber by efficiently catalyzing ceramization on fluorophlogopite. *Compos Commun* 2021, **25**: 100683.

[31] Liu JS, Dong SJ, Zhu LP, *et al.* Preparation, luminescence and potential application of rare earth Sm^{3+}-doped fluorphlogopite phosphors. *J Lumin* 2022, **244**: 118685.

[32] Liu JS, Qi N, Dong SJ, *et al.* Solid state reaction preparation of $BaMg_2Si_4O_{10}F_2$: Eu^{3+} synthetic-mica phosphor for latent fingerprint identification. *Ceram Int* 2024, **50**: 2931–2938.

[33] Information on https://www.webelements.com/ and http://abulafia.mt.ic.ac.uk/shannon/ptable.php.

[34] Panda R, Behera M, Kumar RA, *et al.* Luminescence studies of high color purity red-emitting $CaAl_4O_7:Eu^{3+}$ phosphor prepared by microwave-assisted synthesis technique. *J Alloys Compd* 2023, **968**: 171879.

[35] Li S, Hu W, Brik MG, *et al.* Achieving highly thermostable red emission in singly Mn^{2+}-doped $BaXP_2O_7$ (X = Mg/Zn) via self-reduction. *Inorg Chem Front* 2022, **9**: 3224–3232.

[36] Wang B, Kong YC, Chen ZK, *et al.* Thermal stability and photoluminescence of Mn^{2+} activated green-emitting feldspar phosphor $SrAl_2Si_2O_8$:Mn^{2+} for wide gamut w-LED backlight. *Opt Mater* 2020, **99**: 109535.

[37] Yang JQ, Zhou YY, Ming H, *et al.* Site-selective occupancy of Mn^{2+} enabling adjustable red/near-infrared multimode luminescence in olivine for dynamic anticounterfeiting and encryption. *ACS Appl Electron Mater* 2022, **4**: 831–841.

[38] Dorenbos P. Energy of the first $4f^7 \rightarrow 4f^65^d$ transition of Eu^{2+} in inorganic compounds. *J Lumin* 2003, **104**: 239–260.

[39] Zou JH, Li LJ, Chen JY, *et al.* Eu^{2+}-doped oxyfluoride glass scintillator for X-ray imaging. *J Alloys Compd* 2025, **1020**: 179428.

[40] Wang JH, Dong LL, Lyu ZY, *et al.* Facile synthesis of highly efficient and thermally stable $BaAl_4Sb_2O_{12}$:Eu^{2+} phosphor in air. *Adv Funct Mater* 2023, **33**: 2214611.

[41] Blasse G. On the nature of the Eu^{2+} luminescence. *Phys Status Solidi B* 1973, **55**: K131–K134.

[42] Shi SK, Liu XR. The narrow line emission of the f–f transition of Eu^{2+} in $Ba_{1-x-y}Eu_xGd_yMgF_{4+y}$ complex fluorides. *Chin J Chem Phys* 1998, **11**: 206–210. (in Chinese)

[43] He J, Cai NH, Fu LS, *et al.* Sensitization of Mn^{2+} luminescence by Eu^{2+}: A combined study using optical spectroscopy and luminescence dynamics simulations. *Inorg Chem* 2022, **61**: 1745–1755.

[44] Yin ZQ, Mao YF, Shi SK, *et al.* Solution combustion synthesis of high-entropy rare earth oxide $Ce_{0.2}La_{0.2}Gd_{0.2}Y_{0.2}Lu_{0.2}O_{1.6}$:$Eu^{3+}$ phosphor with intense blue-light excitable red emission for solid-state lighting. *J Adv Ceram* 2024, **13**: 1852–1860.

[45] Paulose PI, Jose G, Thomas V, *et al.* Sensitized fluorescence of Ce^{3+}/Mn^{2+} system in phosphate glass. *J Phys Chem Solids* 2003, **64**: 841–846.

[46] Xiao WQ, Lei F, Yin LQ, *et al.* Solid state synthesis, luminescent properties and energy transfer from Eu^{2+} to Mn^{2+} in red phosphor $BaMg_2Si_2O_7$: Eu^{2+}, Mn^{2+}. *Solid State Sci* 2017, **72**: 116–123.

[47] Cao ZY, Wu JY, Shi SK, *et al.* Efficiently enhanced deep-red emission of Ba_3WO_6:Mn^{4+} oxide phosphor *via* the Gd^{3+} incorporation. *Ceram Int* 2023, **49**: 1409–1418.

[48] Wu JY, Yin ZQ, Shi SK, *et al.* An Al^{3+}-incorporated Ca_2LuNbO_6:Mn^{4+} oxide phosphor with dramatic deep-red and far-red emission bands. *J Mater Chem C* 2023, **11**: 15731–15741.

[49] Cao ZY, Dong SJ, Shi SK, *et al.* Solid state reaction preparation of an efficient rare-earth free deep-red Ca_2YNbO_6:Mn^{4+} phosphor. *J Solid State Chem* 2022, **307**: 122840.

[50] Dong Q, Yang JJ, He SG, *et al.* Realizing near-UV light excitation of Mn^{2+} via efficient energy transfer from Eu^{2+} for white LEDs. *Mater Res Bull* 2020, **125**: 110789.

[51] van Bunningen AJ, Sontakke AD, van der Vliet R, *et al.* Luminescence temperature quenching in Mn^{2+} phosphors. *Adv Opt Mater* 2023, **11**: 2202794.

[52] Zhou ZW, Zheng JM, Shi R, *et al. Ab initio* site occupancy and far-red emission of Mn^{4+} in cubic-phase $La(MgTi)_{1/2}O_3$ for plant cultivation. *ACS Appl Mater Inter* 2017, **9**: 6177–6185.